Aligning and orienting molecules trapped in octahedral crystal fields

Toni Kiljunen,[1] Burkhard Schmidt,[2] and Nikolaus Schwentner[1]

[1]*Institut für Experimentalphysik, Freie Universität Berlin, Arnimallee 14, D–14195 Berlin, Germany*

[2]*Institut für Mathematik II, Freie Universität Berlin, Arnimallee 2–6, D–14195 Berlin, Germany*

(Dated: August 29, 2005)

Abstract

The effect of external fields on directional states of a linear molecule trapped in a crystal field of octahedral symmetry is studied numerically. Adiabatic field-dressed energy levels are obtained by solving the time-independent Schrödinger equation for the rotational degrees of freedom of the confined molecule. In the absence of external fields, the internal, octahedral crystal field serves to transform free-rotor states to angularly confined librational states of defined parity which arrange in near-degenerate sets of high multiplicity. Interaction of a linearly polarized, nonresonant laser field with the polarizability or of a static electric field with the dipole moment create alignment or orientation of the molecular axis, respectively. In the latter case, the combined effect of internal (octahedral) and external static field is instrumental in creating orientation by coupling different tunneling states. Depending on the polarization direction of the external fields with respect to the symmetry axes provided by the crystal field, cooperative and competitive effects are distinguished. If the direction of the external field coincides with the minima of the crystal field, high degrees of alignment or orientation can be achieved for specific states, even for low field strengths. Otherwise, high efficiency of this mechanism is restricted to high fields and low temperatures. Strategies for an experimental realization are outlined.

PACS numbers: 33.80.-b, 42.50.Vk, 71.70.Ch, 82.50.-m, 33.15.Bh, 33.20.-t

I. INTRODUCTION

Efforts in molecular alignment and orientation are highly motivated by noting that many chemical reactions depend crucially on the relative orientation of the reactants [1, 2]. In creating a certain alignment or orientation, one needs to rotate the molecules, which is closely connected to other research fields where the manipulation of external degrees of freedom plays a decisive role, e.g., in molecular scale devices like switches and motors [3–5]. Alignment is also a necessary precondition in tomographic imaging of molecular orbitals by intense laser pulses [6, 7]. A related, complementary technique applicable for aligned or oriented molecules is recently established for sub-femtosecond temporal resolution of molecular structure [8, 9].

There is a long line of studies of successful theoretical and experimental work on the manipulation of molecular alignment in the gas phase, for a review see Ref. [10]. A robust and efficient mechanism proceeds via intense, near- or nonresonant laser fields. The interaction with the anisotropic polarizability of a molecule induces a dipole moment which, in turn, causes a coupling to the external field [11–15]. The resulting pendular states are superpositions of the field-free rotor states and the molecular axis librates about the polarization direction of the field [16, 17]. These states occur in pairs of different parity which are connected by tunneling through the barrier provided by the light-induced potential. If, in addition, a static field is applied, oriented molecular states can be formed as superpositions of tunneling pairs of pendular states [18, 19]. This concept has been experimentally realized for molecules both in gas phase [20, 21] and in small rare gas clusters [22, 23]. For the combined fields, the necessary electric field strengths may be much lower than in the pendular orientation approach using static fields alone [1, 24].

In contrast, the manipulation of rotational states of molecular impurities embedded in solid state matrices is yet an essentially unexplored field. The main difference is that the rotational motion of molecules in solid matrices is governed by an internal field, often referred to as crystal field, describing the interaction with the surroundings. Upon increasing its strength, the rotational motion becomes more and more hindered. Finally, the molecular rotational states approach the limit of librational states describing angular oscillations about preferred crystallographic axes [25, 26]. Correspondingly, the J-level degeneracies $g = 2J+1$ of the free-rotor states are lifted as hindered rotor states $A(g = 1)$, $E(g = 2)$, and $T(g = 3)$

of cubic symmetry are formed in combinations of $|J, M\rangle$ states [27]. For a very strong crystal field, these levels group together in states with again high multiplicities defined by the librational quantum number $n = 0, 1, \ldots$ so that the degeneracies become $g = 6(n + 1)$, $g = 8(n + 1)$, or $g = 12(n + 1)$ for the n-th librationally excited state with $\langle 100 \rangle$, $\langle 111 \rangle$, or $\langle 110 \rangle$ directionality, respectively. In between these limiting cases the states are found in near-degenerate sets asymptotically correlating to a librational state. In analogy to the case of gas phase molecules, interconversion between the states is possible by means of two-dimensional tunneling in the plane spanned by the angular coordinates [28]. In the following, the manipulation of the rotational motion of molecules in crystals by resonant or nonresonant fields can be categorized by the following limits: Fields are termed as strong if they can achieve notable mixing of states belonging to different multiplets, while weak fields can only mix states inside a single multiplet. Equivalently, in the first case systems are driven above rotational barriers, while they can tunnel through the barriers in the second case. In analogy, temperatures are considered as high or low, if the thermal energies are sufficient or insufficient to overcome rotational barriers, respectively. Accordingly, the statistical Boltzmann weights of states within a multiplet are approximately equal or notably different for high or low temperatures, respectively.

The case of intense-field alignment of molecules in octahedral matrices has been investigated in our previous study [29]. On the one hand, there may be competition between internal (crystal) and external (light-induced) fields if the polarization of the external field does not coincide with one of the preferred crystallographic axes. On the other hand, the crystal field may also lead to enhancement of alignment compared to a free rotor, if the two fields cooperate. In the present work we extend the preliminary studies of Ref. [29] in two directions: In addition to a more detailed investigation of alignment considering polarization along different lattice directions, we explore the possibility for orientation of molecules in matrices. To this end, we proceed in analogy to the above described combined effect, where gas phase molecules are simultaneously subject to both intense radiative and weak static fields [18–23]. For the molecule embedded in a solid, we show that the use of two simultaneous external fields is not necessary: Instead, the internal matrix field can play a similar role as the alignment field in providing the tunneling multiplets of pendular states. Those can be manipulated by a weak static field to induce orientation effects. In particular, it is expected that for increasing internal field the tunneling splitting among librational states

decreases, thus reducing the required static field strengths to values far below those required for pendular orientation. The efficiency of both the alignment and orientation through the laser and static fields, respectively, competes with thermal averaging. We investigate the desired effects not only assuming specific initial states, but the results are computed for different temperatures also, concentrating on low-temperature ensembles, i.e., the energetically lowest multiplet correlating with ground librational state.

In this article, Sec. II presents a simplified model for a confined linear rotor interacting with the crystal, alignment, and static fields, and describes the solution of the time-independent Schrödinger equation using symmetry-adaption techniques. Then, the adiabatic properties of eigenstates in the chosen octahedral field are described for the rotor–librator in the absence of external fields (Sec. III). The resulting rotational densities are manipulated by external fields, first for alignment in Sec. IV and then for orientation in Sec. V. Field-induced shifts of energy levels are presented along with discussion on the property expectation values, and conclusions are drawn finally in Sec. VI, where also the experimental feasibility is discussed.

II. COMPUTATIONAL METHOD

We consider a linear molecule in an electronically nondegenerate $^1\Sigma$ state translationally caged by a cubic crystal field of octahedral symmetry. This is often realized for impurities which are small enough to fit in a mono-substitutional lattice site such that their rotational motions are only moderately influenced by the surroundings. For instance, hydrogen halides or other small diatomic molecules in solid rare gases [30, 31], in alkali halide crystals [32, 33], or at interstitial sites of the fullerite [34, 35] come into question.

The confined (heteronuclear, prolate) molecule exhibits a permanent dipole moment μ along the molecular axis, and has polarizability components parallel ($\alpha_\parallel$) and perpendicular ($\alpha_\perp$) to it ($\Delta\alpha = \alpha_\parallel - \alpha_\perp > 0$). The molecule is subject either to an intense, nonresonant laser field $\mathcal{E}_\mathrm{L}$ or to a weak, static electric field $\mathcal{E}_\mathrm{S}$. The linear polarization direction of the nonresonant or static field is varied such that it lies along one of $\langle 100\rangle$, $\langle 111\rangle$, or $\langle 110\rangle$ crystallographic axes (class of symmetry equivalent directions). The interaction then depends on the polar angle θ between the molecular axis and the field direction defining the laboratory frame, and on the orientation of the solid cage frame (θ', ϕ') with respect to it.

We write the time-independent Hamiltonian for the embedded molecule as

$$\hat{H}/B = (\hat{\mathbf{J}}/\hbar)^2 + \hat{V}_\kappa + \hat{V}_\alpha + \hat{V}_\mu \,, \tag{1}$$

and thereby neglect the coupling of rotational and translational motion of the impurity molecule [36, 37]: The molecular center of mass (c.m.) is fixed at a substitutional lattice site, and $\hat{\mathbf{J}}$ is the angular momentum operator having its origin at the c.m. Furthermore, translational motion of the c.m. is neglected in the model as we assume that the center of interaction (c.i.) coincides with the c.m. Eccentric motion about a fixed c.i. can, however, be accounted for by an appropriate down-scaling of the rotational constant $B = \hbar^2/(2I)$ [38, 39]. For the temperatures involved in the present work, the rotations can not couple effectively to either vibrations [4] or electronic excitations of the guest (rotronic coupling, [40]). Moreover, we neglect any coupling between the external fields and the surrounding matrix. This is justified for rare gases as long as the intensities are below specific breakthrough and damage thresholds.

We present the octahedral potential due to the solid surrounding as

$$V_\kappa(\theta', \phi'; \kappa) = \kappa \left[K_4 V_4(\theta', \phi') + K_6 V_6(\theta', \phi') \right] \,, \tag{2}$$

where κ is a strength parameter, K_4 and K_6 values determine the shape, and the angular functions $V_4(\theta', \phi')$ and $V_6(\theta', \phi')$ are surface harmonics of the O_h point group (see Sec. III). We concentrate solely on the angular degrees of freedom (θ', ϕ') of the guest molecule and neglect possible deformations of the matrix in accommodating the impurity. This approximation complements the earlier work [38, 41–44] where the radial coordinate has played a major role in coupling the guest motions to various host modes.

The laser interaction part leads to the effective, instantaneous potential of form

$$V_\alpha(\theta; \Delta\omega) = -(\Delta\omega \cos^2\theta + \omega_\perp) \,, \tag{3}$$

and the potential in the static field is given by

$$V_\mu(\theta; \omega) = -\omega \cos\theta \,. \tag{4}$$

The interaction parameters used are dimensionless [18]: $\omega_{\parallel,\perp} = \mathcal{E}_\mathrm{L}^2 \alpha_{\parallel,\perp}/(4B)$ with $\Delta\omega = \omega_\parallel - \omega_\perp$, κ is in units of B, and $\omega = \mu\mathcal{E}_\mathrm{S}/B$. As usual [19], the additive constant $\omega_\perp$ is omitted in Eq. (3). For practical units, the conversions are: $\mathcal{E}_\mathrm{S}[\mathrm{kV\,cm^{-1}}] = \omega B[\mathrm{cm^{-1}}]/(0.0168\,\mu[\mathrm{Debye}])$ and $\mathcal{I}_0[\mathrm{W\,cm^{-2}}] = \Delta\omega B[\mathrm{cm^{-1}}]/(10^{-11}\Delta\alpha[\mathrm{\AA}^3])$.

TABLE I: Correlation table for the octahedral (O_h) point group and its subgroups obtained for nonresonant polarizability interaction ($D_{\infty\mathrm{h}}$) with light polarized along fourfold $\langle 100\rangle$, threefold $\langle 111\rangle$, and twofold $\langle 110\rangle$ axes of symmetry. Correlations for the ungerade (u) representations are obtained by replacing indices g with u throughout the table.

O_h	$D_{4\mathrm{h}}$ $\langle 100\rangle$	$D_{3\mathrm{d}}$ $\langle 111\rangle$	$D_{2\mathrm{h}}$ $\langle 110\rangle$
$A_{1\mathrm{g}}$	$A_{1\mathrm{g}}$	$A_{1\mathrm{g}}$	$A_{1\mathrm{g}}$
$A_{2\mathrm{g}}$	$B_{1\mathrm{g}}$	$A_{2\mathrm{g}}$	$B_{1\mathrm{g}}$
E_g	$A_{1\mathrm{g}} + B_{1\mathrm{g}}$	E_g	$A_{1\mathrm{g}} + B_{2g}$
$T_{1\mathrm{g}}$	$A_{2\mathrm{g}} + E_\mathrm{g}$	$A_{2\mathrm{g}} + E_\mathrm{g}$	$B_{2\mathrm{g}} + B_{1\mathrm{g}} + B_{3\mathrm{g}}$
$T_{2\mathrm{g}}$	$B_{2\mathrm{g}} + E_\mathrm{g}$	$A_{1\mathrm{g}} + E_\mathrm{g}$	$A_{1\mathrm{g}} + B_{1\mathrm{g}} + B_{3\mathrm{g}}$

The Schrödinger equation corresponding to Eq. (1) is solved in spherical harmonics basis $\{Y_{J,M}(\theta,\phi)\}$ with $J_\mathrm{max} = 26$. The interaction matrices consist exclusively of elements of type $\langle Y_{J,M}|Y_{l,m}|Y_{J',M'}\rangle$ which allows for convenient analytic evaluation with the Gaunt formula derived from the Clebsch–Gordan series [45]. To reduce the size of the basis set, symmetry adaption techniques are employed [46–48]. In particular, only symmetry-adapted surface harmonics of the same irreducible representation are coupled by a totally symmetric Hamiltonian. While the crystal field alone possesses octahedral (O_h) symmetry, the symmetry is lowered in the presence of interaction with external fields. The correlations for the appropriate subgroups of the crystal O_h are shown in Tables I and II. When needed for clarity in the text, we give the parent representation belonging to O_h in parentheses after the symbol, i.e., $A_1(E_\mathrm{g})$ means that this A_1 originates from the E_g representation in zero external fields.

III. LIBRATION IN THE OCTAHEDRAL POTENTIAL

Because the main observables in the present work are the $\langle\cos^2\theta\rangle$ for alignment and $\langle\cos\theta\rangle$ for orientation, characterized by the angle θ between the molecular axis and the field polarization vector, it is convenient to work in space-fixed reference frame defined by the external field, and expand the rotational wave functions in these laboratory coordinates. The external fields (discussed in Secs. IV and V) are applied in three different directions [001],

TABLE II: Same as Table I but for static dipole interaction ($C_{\infty v}$). Correlations for the ungerade (u) representations are obtained by interchanging indices 1 and 2 for the subgroup representations.

O_h	C_{4v} $\langle 100\rangle$	C_{3v} $\langle 111\rangle$	C_{2v} $\langle 110\rangle$
A_{1g}	A_1	A_1	A_1
A_{2g}	B_1	A_2	B_1
E_g	$A_1 + B_1$	E	$A_1 + B_1$
T_{1g}	$A_2 + E$	$A_2 + E$	$A_2 + B_1 + B_2$
T_{2g}	$B_2 + E$	$A_1 + E$	$A_1 + A_2 + B_2$

TABLE III: Weight factors (K_4, K_6) and rotated octahedral potential components (V_4, V_6) with light field polarized along a fourfold $\langle 100\rangle$, threefold $\langle 111\rangle$, or twofold $\langle 110\rangle$ axis of symmetry. Expansion in laboratory coordinate spherical harmonics $Y_{J,M}(\theta,\phi) = (-1)^M\sqrt{\frac{2J+1}{4\pi}}\sqrt{\frac{(J-M)!}{(J+M)!}}P_J^M(\cos\theta)\mathrm{e}^{iM\phi}$ for $M \geq 0$ and P_J^M are the associated Legendre polynomials. For negative M holds: $Y_{J,-M}(\theta,\phi) = (-1)^M Y^*_{J,M}(\theta,\phi)$. Note that this convention differs from that used in Ref. [48].

K_4		$-52\sqrt{\pi}/(11\sqrt{21})$
	[001]	$\frac{1}{6}[\sqrt{21}\,Y_{4,0} + \sqrt{15/2}\,(Y_{4,4} + Y_{4,-4})]$
$V_4(\theta',\phi')$	[111]	$\frac{1}{9}[-\sqrt{21}\,Y_{4,0} + \sqrt{30}\,(Y_{4,3} - Y_{4,-3})]$
	[110]	$\frac{1}{24}[-\sqrt{21}\,Y_{4,0} - \sqrt{210}\,(Y_{4,2} + Y_{4,-2}) + 3\sqrt{15/2}\,(Y_{4,4} + Y_{4,-4})]$
K_6		$16\sqrt{\pi}/(11\sqrt{26})$
	[001]	$\frac{1}{4}[\sqrt{2}\,Y_{6,0} - \sqrt{7}\,(Y_{6,4} + Y_{6,-4})]$
$V_6(\theta',\phi')$	[111]	$\frac{1}{54}[24\sqrt{2}\,Y_{6,0} - \sqrt{420}\,(Y_{6,3} - Y_{6,-3}) + \sqrt{462}\,(Y_{6,6} + Y_{6,-6})]$
	[110]	$\frac{1}{64}[-26\sqrt{2}\,Y_{6,0} + \sqrt{210}\,(Y_{6,2} + Y_{6,-2}) + 5\sqrt{28}\,(Y_{6,4} + Y_{6,-4}) + \sqrt{462}\,(Y_{6,6} + Y_{6,-6})]$

[111], and [110] with respect to the confining crystal. Therefore, the internal crystal-field potential expressed by the two lowest order nontrivial surface harmonics V_4 and V_6 of O_h point-group symmetry must be rotated accordingly. This is achieved by use of the Wigner rotation matrices [45] and the results are given in Table III.

Different hindering potential shapes for rotation occur in solid-state matrices, and thereby

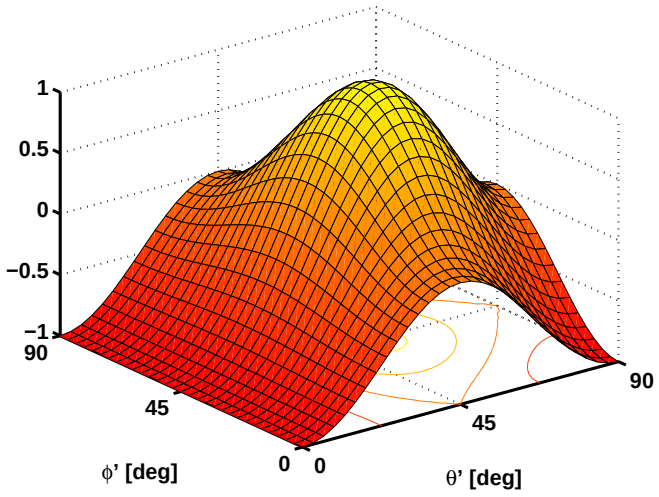

FIG. 1: (Color online) The octahedral model potential $V_\kappa(\theta', \phi')/\kappa$ with minima at the $\langle 100 \rangle$, saddle points at the $\langle 110 \rangle$, and maxima at the $\langle 111 \rangle$ axes of symmetry. The external fields are applied along [001] ($\theta' = 0$), [110] ($\theta' = \pi/2$, $\phi' = \pi/4$), or [111] ($\theta' = \cos^{-1} 1/\sqrt{3}$, $\phi' = \pi/4$) directions.

various directional states can exist. The potential given by Eq. (2) resembles the Devonshire model ($K_6 = 0$) [27, 28, 40, 49, 50] in that the minima occur in the six $\langle 100 \rangle$ directions with $V_{\rm min}/\kappa = -1$. However, the two-parameter construction including V_6 sets the saddle point energy in the twelve $\langle 110 \rangle$ directions to zero, independent of κ (Devonshire: 1/4). Potential energy maxima are found in the eight $\langle 111 \rangle$ directions with $V_{\rm max}/\kappa = 10/9$ (Devonshire: 2/3). The first octant of the potential is plotted in Fig. 1. Here, the laboratory coordinate frame (θ, ϕ) coincides with the single crystal frame (θ', ϕ') and minima are found at $\theta = 0$ or π; $\theta = \pi/2$, $\phi = 0$, $\pm\pi/2$ or π. Consequently, the model potential tends to arrange the rotational density along the $\langle 100 \rangle$ directions. For increasing strength of the crystal field, more rotational states become bound with respect to the barriers at $\langle 110 \rangle$ ($E_n(\kappa) < 0$) and at $\langle 111 \rangle$ ($E_n(\kappa) < 10\kappa/9$), see Fig. 2. We assign the states $V_{\rm min} < E_n \leq 0$ to a librator and the states $0 < E_n \leq V_{\rm max}$ to a hindered rotor. Note that also for the higher states $E_n > V_{\rm max}$ the energies and shapes of the rotational densities are affected, however, they are not restricted to occupy preferred directions only. The zero potential line essentially distinguishes the tunneling regime from classical rotations for directional changes of a molecule. Our choice for Eq. (2) corresponds to the simplest (lowest multiplicity, $g = 6$) case for presenting the directional nature of the librational states in octahedral fields [28, 49].

The calculated energy levels $E_n(\kappa; V_\alpha = V_\mu = 0)$ in Fig. 2 depict the correlation from a freely rotating ($\kappa = 0$) to a librating molecule. The potential minimum, saddle height, and maximum energies are indicated by the dashed lines for classifying the nature of rotational states. Considering a transition of a molecule from one minimum energy orientation to another, the regime below the zero potential line belongs to tunneling, whereas the above states are angularly delocalized and molecules experience rather a rotational diffusion type mechanism. The set of three lowest levels with symmetries of A_{1g} (circles), T_{1u} (points), and E_g (squares) correlate to the $J = 0, 1, 2$ free-rotor states, respectively. A rotational density plot corresponding to the lowest energy component A_{1g} is inserted to present the angular confinement at $\kappa = 25$. The lobes of the three dumb-bells lie along the x, y, z coordinate axes in the (Cartesian) reference frame of the crystal. The other densities within the lowest energy librational manifold map the same angular space but each of them does so partially: Each T_{1u} is a single dumb-bell (cylindrical symmetry). The $T_{1u,3}$ density, for instance, occupies the z axis directions only as it exclusively consists of $|J, M = 0\rangle$ states. The E_g states can be schematically written as $E_{g,1} = |2, \pm 2\rangle + |4, \pm 2\rangle + |6, \pm 2\rangle + |6, \pm 6\rangle \ldots$, i.e., two dumb-bells spanning the horizontal (x, y) plane, and $E_{g,2} = |2, 0\rangle + |4, 0\rangle + |4, \pm 4\rangle \ldots$, i.e., similar to the drawn A_{1g} but the vertical dumb-bell is emphasized over the two in perpendicular plane.

Next, we consider a cut at $\kappa = 25$ where only the sixfold, nearly degenerate ground state (three closely separated tunneling states A_{1g}, T_{1u}, and E_g) at $E \approx -7B$ (zero-point energy $E_{ZP} \approx 18B$) is close to librational limit while the higher states belong to hindered rotors. The energy gap to these states (crystal-field splitting) is more than $13B$. In contrast, the tunneling splitting is much smaller: $0.71B$ for A_{1g}–T_{1u} and $0.43B$ for T_{1u}–E_g. The rotational density of A_{1g} ground state is drawn in Fig. 2. Corresponding expansion coefficients of the state vector in terms of D_{4h}, D_{3d}, or D_{2h} subgroup surface harmonics given in Table IV are qualitatively similar to those of the V_4 potential function compiled in Table III.

In the following, we define a reduced rotational temperature $\mathcal{T}$ with $T[\mathrm{K}] = 1.44\mathcal{T}B[\mathrm{cm}^{-1}]$ and restrict it to 1 or 10 k_B/B throughout the remainder of this article. For the lower reduced temperature $\mathcal{T} = 1$ we have Boltzmann factors $1\times 0.32(A_{1g})$, $3\times 0.16(T_{1u})$, and $2\times 0.10(E_g)$ in the three lowest levels, i.e., 100% of population is found in the lowest near-degenerate set of states correlating to the librational ground state. For the higher reduced temperature $\mathcal{T} = 10$ similarly 0.12, 0.11, and 0.10 are found amounting to 65% of population in that manifold.

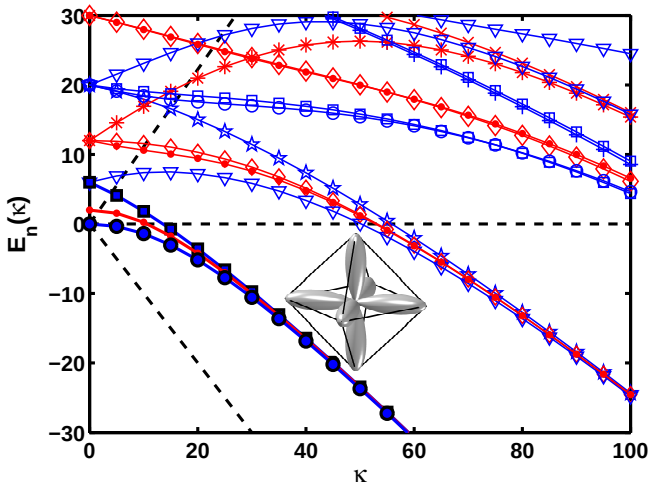

FIG. 2: (Color online) The energy spectrum $E_n(\kappa)$ for the confined molecule in the octahedral field. The symbols denote $O_{\rm h}$ irreducible representations as follows: $A_{1\rm g}$ (circles), $T_{1\rm u}$ (points), $E_{\rm g}$ (squares), $T_{2\rm g}$ (triangles), $T_{2\rm u}$ (diamonds), $A_{2\rm u}$ (asterisks), $T_{1\rm g}$ (five-pointed stars), $E_{\rm u}$ (crosses), and $A_{2\rm g}$ (pluses). The dashed lines show the extrema of the potential. E_n and κ are in units of B. Ground state rotational density for $\kappa = 25$ is inserted in the octahedron. (g and u parities are distinguished with blue and red symbols, respectively)

In the following sections we demonstrate how the external fields affect the rotational density distributions of ground librational states. To this end we choose this significant strength $\kappa = 25$ for the crystal field, because we expect that the crystal-field splitting is sufficiently large to survive random stresses in reality. These may arise from thermal motions or other deviations from perfect symmetry. In contrast, the fragile tunneling structure among the levels may get smeared out by already small distortions [28].

IV. LASER-INDUCED ALIGNMENT IN CRYSTAL FIELDS

When an intense, nonresonant alignment field is applied to molecules, here confined by the crystal field, the interaction is given by V_α which is proportional to $\cos^2\theta$. The dependence of energy levels $E_n(\Delta\omega;\kappa = 25)$ on $\Delta\omega$ is shown in Fig. 3. We present the six levels corresponding to the librational ground state and those upper states that contribute to avoided crossings with these energy levels.

The upmost panel of Fig. 3 depicts the case that we call cooperative [29], where the

external field is along a $\langle 100 \rangle$ direction. There, two of the density lobes already occupy the target directions [states $1A_{1g}$ (circles) and A_{2u} (triangles)] defined by the field and thus gain energy as the interaction strength $\Delta\omega$ increases. The density becomes gradually squeezed along the field. The other four states perpendicular to the field remain essentially unaffected by the $\cos^2\theta$ type interaction. In order to change the directional property of these perpendicular states [$2A_{1g}$ (circles), $1, 2E_u$ (diamonds) and B_{1g} (squares)] one has to increase the field until higher states with the same symmetry come into avoided crossings. Upon passing the avoided crossings at $\Delta\omega = 25$ and 45, the states change their characters abruptly rather than narrowing smoothly as is observed for the parallel states. In order to understand the directional properties of the rotational states subject to the nonresonant alignment field, one has to consider the effective potential $V_\kappa + V_\alpha$. The height $V_b = -\Delta\omega/2$ of its barrier occurring at $\theta' = \pi/4$, $\phi' = 0, \pi/2$ between the target direction and the perpendicular plane, see Fig. 1, is also drawn in the upper panel of Fig. 3.

In the competitive case with the field along a $\langle 111 \rangle$ direction, alignment is achieved by turning the density onto the crystal-field maxima, see the middle panel of Fig. 3. All the states [A_{1g} (circles), A_{2u} (triangles), E_u (squares), and E_g (diamonds)] exhibit similarly some degree of alignment upon strengthening the interaction. No abrupt changes occur and the avoided crossings around $\Delta\omega \approx 30$ are barely visible. On the contrary, when the field is along a $\langle 110 \rangle$ as in the lowest panel of the figure, two clear avoided crossings occur at $\Delta\omega = 25$–30 (for $2A_{1g}$, circles) and $\Delta\omega = 35$–40 (for B_{2u}, diamonds). These are the perpendicular states, whereas the other four states [$1A_{1g}$ (circles), B_{1u} (right-triangles), B_{3u} (down-triangles), and B_{2g} (squares)] exhibit density maxima at $\theta = \pi/4$ for $\Delta\omega = 0$ and, hence, become more easily aligned.

Insertions in Fig. 3 depict the rotational densities at $\Delta\omega = 60$ for the energetically lowest states A_{1g}, except for D_{4h} panel where the second root $2A_{1g}$ is shown. In this case, the density is plotted for the state beyond the avoided crossing, and it exhibits alignment which is inherited from the higher state. We note that the field is applied vertical in all the panels. As in the gas phase [19], the energies of the lowest states arrange to closely separated gerade–ungerade pairs. For the ground state doublet Ψ_g, Ψ_u the expansion coefficients > 0.1 are tabulated in Table IV. For comparison, the ground state for vanishing alignment field ($\Delta\omega = 0$) is also shown. The effect of the alignment field is to introduce $M = 0$ character into a wave function, i.e., to mix in components of the other states parallel to the field ($\theta = 0, \pi$). This

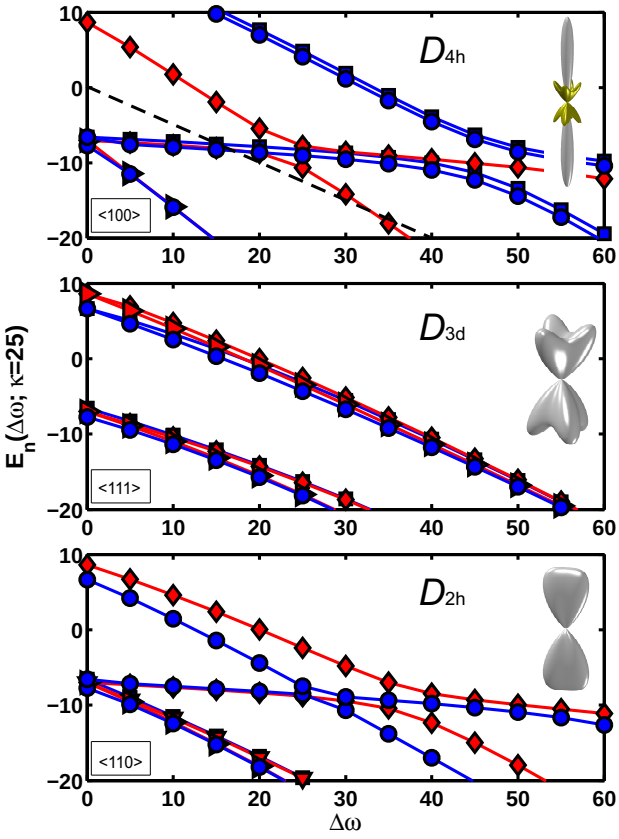

FIG. 3: (Color online) Reduced energy spectrum $E_n(\Delta\omega;\kappa = 25)$ of a confined molecule when alignment field V_α is applied in three directions with respect to the crystal axes: $\langle 100\rangle$ – potential minimum, $\langle 111\rangle$ – potential maximum, and $\langle 110\rangle$ – saddle point. Common to all panels, the totally symmetric A_{1g} components are marked by circles, see text for others. Aligned densities are inserted beyond avoided crossings ($\Delta\omega = 60$) with field direction set vertical in the plots. Saddle point energy $V_b(\Delta\omega)$ is shown by dashed line in D_{4h} case. (blue – gerade states, red – ungerade states)

happens either directly via the nonresonant field (inducing $\Delta J = \pm 2, \Delta M = 0$ transitions) or via the field-induced avoided crossings of the energy levels. The former mechanism is evident for the ground state doublets listed in Table IV, whereas the latter takes place in the case of, e.g., $2A_{1g}$ of D_{4h} plotted in the upper panel of Fig. 3. There, the perpendicular components, e.g., $|4, \pm 4\rangle$, disappear from the state vector upon passing the avoided crossing ($\Delta\omega$ = 35–55) and signs of $|J, 0\rangle$ components become constructive. Hence, the alignment

TABLE IV: The $|J,M\rangle$ wave function components (with > 0.1 expansion coefficients) for the ground state doublets $\Psi_{\rm g}$,$\Psi_{\rm u}$ at $\kappa = 25$, $\Delta\omega = 60$. Ψ_0 is the totally symmetric ground state at $\kappa = 25$, $\Delta\omega = 0$. Abbreviation $|J,M\rangle^{\pm} \equiv |J,M\rangle \pm |J,-M\rangle$.

	$D_{4\rm h}$	$D_{3\rm d}$	$D_{2\rm h}$
$\Psi_{\rm g}$	$0.42\|0,0\rangle$	$-0.71\|0,0\rangle$	$-0.56\|0,0\rangle$
	$0.71\|2,0\rangle$	$-0.67\|2,0\rangle$	$-0.71\|2,0\rangle$
	$0.50\|4,0\rangle$	$-0.11\|4,3\rangle^{-}$	$-0.24\|4,0\rangle$
	$0.24\|6,0\rangle$	$0.11\|6,0\rangle$	$0.19\|4,2\rangle^{+}$
			$0.11\|6,2\rangle^{+}$
$\Psi_{\rm u}$	$0.66\|1,0\rangle$	$0.93\|1,0\rangle$	$-0.81\|1,0\rangle$
	$0.64\|3,0\rangle$	$0.27\|3,0\rangle$	$-0.47\|3,0\rangle$
	$0.36\|5,0\rangle$	$-0.12\|5,0\rangle$	$0.16\|3,2\rangle^{+}$
	$0.14\|7,0\rangle$	$0.11\|5,3\rangle^{-}$	$0.16\|5,2\rangle^{+}$
Ψ_0	$0.85\|0,0\rangle$	$0.85\|0,0\rangle$	$0.85\|0,0\rangle$
	$0.40\|4,0\rangle$	$-0.27\|4,0\rangle$	$-0.10\|4,0\rangle$
	$0.24\|4,4\rangle^{+}$	$0.32\|4,3\rangle^{-}$	$-0.32\|4,2\rangle^{+}$
			$0.18\|4,4\rangle^{+}$

effect is similar to adding a tetragonal distortion [28], $V_\alpha \propto Y_{2,0}$, i.e., implying an elongation of the cavity (along a $\langle 100\rangle$ in $D_{4\rm h}$ case) which favors the $M = 0$ states.

In order to give a more quantified view of the alignment, we use the expectation value $\langle\cos^2\theta\rangle$. This alignment cosine vanishes for a perpendicular state, is one-third for an isotropic state, and approaches unity for the limit of infinitely narrow wave functions. Instead of evaluating the expectation values explicitly, the values of the alignment cosine can also be readily estimated from the slopes of the energy levels in Fig. 3 by the Hellmann–Feynman theorem

$$\langle\cos^2\theta\rangle_n = -\frac{\partial E_n}{\partial\Delta\omega}\,. \tag{5}$$

The degree of alignment is shown in Fig. 4 (see also Fig. 5) for two thermal ensembles, $\mathcal{T} = 1\,k_{\rm B}/B$ (solid lines), and $\mathcal{T} = 10\,k_{\rm B}/B$ (dashed lines). Moreover, the averaged val-

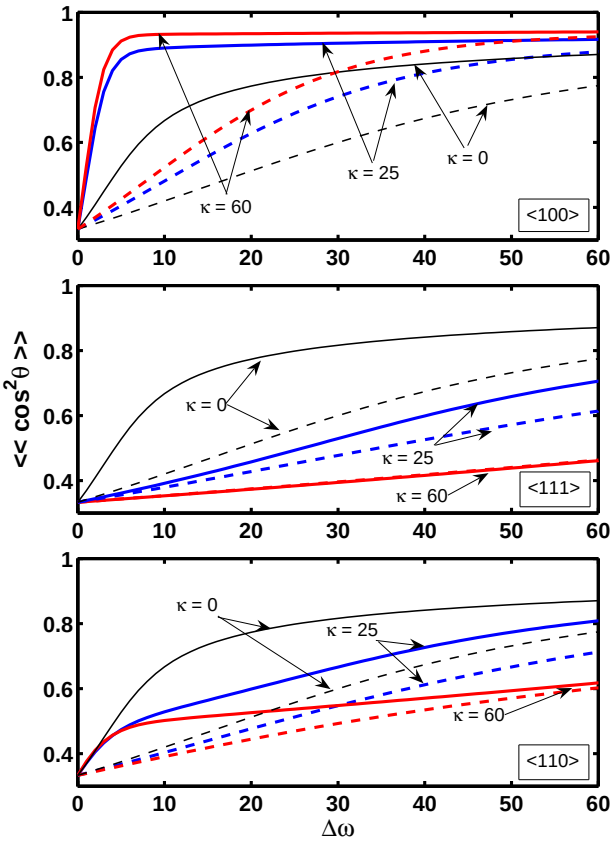

FIG. 4: (Color online) The degree of alignment thermally averaged $\langle\langle\cos^2\theta\rangle\rangle$ when the field (V_α) is applied in three directions and in each for three crystal-field strengths $\kappa = 0$, 25, 60. Solid lines: $\mathcal{T} = 1\,k_{\rm B}/B$, dashed lines: $\mathcal{T} = 10\,k_{\rm B}/B$.

ues $\langle\langle\cos^2\theta\rangle\rangle$ are given for three crystal fields: strength $\kappa = 0$ (free molecule), $\kappa = 25$ (corresponding to the energies in Fig. 3), and $\kappa = 60$.

The upmost panel in Fig. 4 with field along one of $\langle 100\rangle$ directions shows the cooperative effect of the crystal and laser fields on alignment. High degree of alignment is achieved with fields one order of magnitude weaker than in the gas phase ($\kappa = 0$) for the lower temperature case. The enhancement is still significant for the higher temperature $\mathcal{T} = 10\,k_{\rm B}/B$. Comparing to the energy spectrum in Fig. 3, one sees that the average result is insensitive to the dramatic changes of the components at avoided crossings ($\Delta\omega = 25$ and 45). The overall alignment is obtained before coming to these crossings due to the assumed thermally dictated population of the field-induced states. Upon inspecting the effective

superposition potential $V_\kappa + V_\alpha$, we find that the field-insensitive states $2A_{1g}$, $1, 2E_u$, and $1B_{1g}$ are no longer bound to the perpendicular plane for $\Delta\omega \gtrsim 14$ as the potential barrier between the $\theta = \pi/2$ plane and the target $\theta = 0, \pi$ directions has been lowered by $\approx \Delta\omega/2$. The thermal activation for already smaller $\Delta\omega$ is equivalent to an efficient 90-degree tunneling in terms of the crystal field only. The two lower panels in Fig. 4 represent competitive, hindered cases, and the maximal alignment remains below the gas phase values. Now the alignment degree becomes lower in the stronger crystal fields. In the lowest panel, $\Delta\omega \geq 2\kappa$ conditions favor the target direction over the crystal-field minima, whereas $\Delta\omega \geq 19\kappa/6$ is needed to compensate the crystal in the $\langle 111 \rangle$ case (middle panel). In these conditions, however, the angular well is broad and sharply aligned distributions cannot be achieved.

Figure 5 exemplifies further the cooperative effect for laser field polarized along a $\langle 100 \rangle$ discussed above. Here, the alignment is evaluated for the lowest state A_{1g} and compared to the thermal average at $\mathcal{T} = 1\, k_B/B$. The dependence of alignment on the crystal-field strength κ is given for five orders of magnitude in $\Delta\omega$. Within the range of crystal fields studied ($0 < \kappa < 100$) near unity alignment is achieved even for low fields ($\Delta\omega \gtrsim 0.1$). Most significantly, the enhancement with respect to the gas phase ($\kappa = 0$) is visible in the case $\Delta\omega = 1$, which shows also the deviation of the lowest state result (solid line) from the thermal average (dashed). The ground state alignment arises from formation of a gerade–ungerade pair whereas the thermal alignment depends on the Boltzmann balance between the parallel and perpendicular components of the lowest six states. For example, at $\Delta\omega = 10$, the zero-field splitting, i.e., energetic separation of ground state doublet from the higher, perpendicular states, remains as κ is increased, and the thermal average reflects the population of the ground state (A_{1g}, A_{2u}) pair only. For $\Delta\omega = 1$ the perpendicular components gain population upon increasing κ, i.e., upon creating the sixfold degenerate librational ground state; however, small bias for the aligned doublet remains and the thermal average for the alignment cosine can reach a value of 0.54. The weaker fields are not sufficient to overcome Boltzmann averaging and the net alignment remains at the isotropic value.

As a summary of our investigation of alignment by nonresonant laser fields we declare that *weak* fields are sufficient to align single states if κ is large enough and polarization direction is favorable (cooperative case); however, *strong* fields are needed for a thermal ensemble even at a rather low temperature and/or for unfavorable polarizations (competitive case).

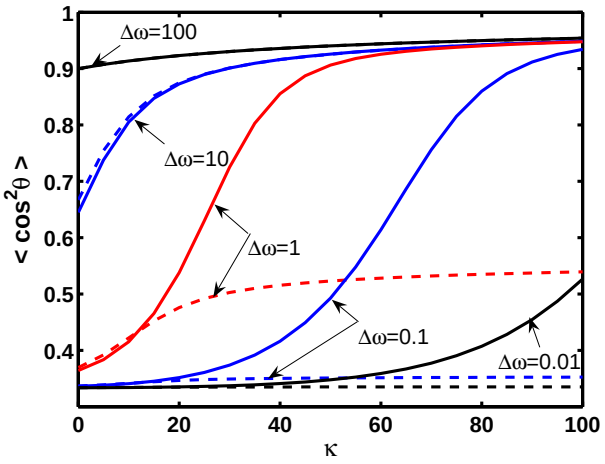

FIG. 5: (Color online) Alignment in the cooperative case with field along a ⟨100⟩: Lowest crystal-field state (A_{1g}, A_{2u} pair) parallel to the field polarization. The thermal averages at $\mathcal{T} = 1\,k_B/B$ are shown by dashed lines.

V. FIELD-INDUCED ORIENTATION IN CRYSTAL FIELDS

In the presence of an external electrostatic field, the interaction with the molecular dipole moment gives rise to the $\cos\theta$ type interaction V_μ. Hence, the degeneracies of the energy levels of the librational states in the octahedral field are partially lifted according to the reduced symmetry C_{nv} $(n = 1, 2, 3)$ of the problem, see Table II. The field dependence of the energy levels $E_n(\omega; \kappa = 25)$ is presented in Fig. 6 for three relative directions between the crystallographic axes and the external field. In addition to states that either stay intact (perpendicular) or gain energy (parallel, high-field seeking), there are now also states that repel the field (antiparallel, low-field seeking states).

In the following, the nature of different states is exemplified in detail for the left column of Fig. 6, where the static field points to the fourfold cube axis and the wave functions are represented by C_{4v} symmetry-adapted spherical harmonics. The lowest state $1A_1(A_{1g})$ becomes essentially parallel and gains energy due to hybridization of the librational crystal-field states. The $2A_1$ and E states in C_{4v}, which are all perpendicular to the field, correlate with the triply degenerate second level T_{1u} in O_h, see Table II. Thus the "z-component" $(M = 0)$ character is transformed to other states. The $B_1(E_g)$ is also perpendicular, whereas the $3A_1(E_g)$ is the repulsive antiparallel state. Inspecting the leading expansion coefficients

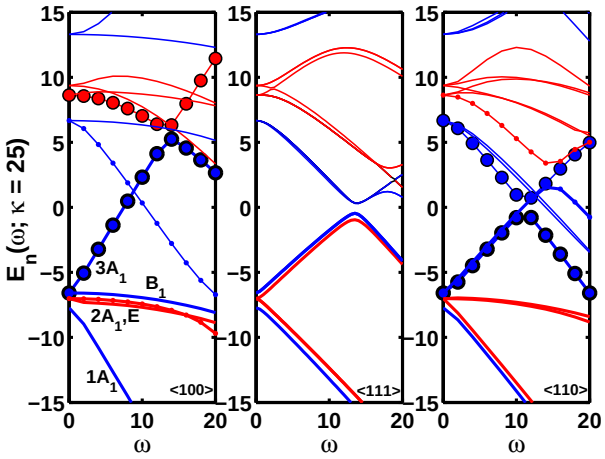

FIG. 6: (Color online) The energy spectrum $E_n(\omega;\kappa=25)$ of a confined molecule when static field V_μ is applied in three directions with respect to the crystal axes. Circular symbols are given to aid resolving the avoided crossings between states with the same symmetry representation. (blue and red distinguish the parent O_h state parities g and u, respectively)

TABLE V: Hybridization of librational states in static external field ($\omega = 10$) showing schematically the composition for the six lowest states of $C_{4\mathrm{v}}$ symmetry in terms of O_h functions ($\omega = 0$). Cooperative case with the static field along a $\langle 100\rangle$ crystallographic axis, see also the labelled curves in the left panel of Fig. 6.

$C_{4\mathrm{v}}$	O_h	Orientation
$1A_1$:	$A_{1\mathrm{g}} + T_{1\mathrm{u,z}} + E_{\mathrm{g},2}$	Parallel
$2A_1$:	$A_{1\mathrm{g}} - E_{\mathrm{g},2}$	Perpendicular
$3A_1$:	$A_{1\mathrm{g}} - T_{1\mathrm{u,z}} + E_{\mathrm{g},2}$	Antiparallel
$(1,2)E$:	$T_{1\mathrm{u,x}} \pm T_{1\mathrm{u,y}}$	Perpendicular
B_1:	$E_{\mathrm{g},1}$	Perpendicular

at $\omega = 10$ and projecting to $\omega = 0$ (O_h), the coupling origins of the lowest six states can be schematically described as given in Table V. The desired orientation parallel to the field is thus obtained only for the lowest of these states. All the other energy levels are undergoing true or avoided crossings as ω is increased. The emphasized curves (circles, points) in Fig. 6 show avoided crossings at $\omega \approx 14$ for the antiparallel $3A_1$ (180-degree turn-over) and $\omega \approx 20$

for the perpendicular E (90-degree flip). The perpendicular states $2A_1$ and B_1 gain only slightly in energy due to the finite width of the density.

The middle panel in Fig. 6 shows the energy spectrum for static field pointing at the threefold cube axis (C_{3v}). Here, the objective is to orient the molecule towards the maximum of the crystal field located $\Delta V = 19\kappa/9$ above the minimum, see Fig. 1. There are three states $A_1(A_{1g})$ and $E(T_{1u})$ turning predominantly parallel and three states $A_1(T_{1u})$ and $E(E_g)$ becoming antiparallel as ω is increased. The antiparallel states turn over at the avoided crossings around $\omega \approx 14$. Beyond this crossing, the rotational wave functions acquire nodes at $\theta = 0, \pi$ and the orientation rather precesses around the target axis direction in this range of ω, since the barrier of the crystal field V_κ to overcome is $\Delta V - E_{ZP}$. In the right panel, where orientation is aimed at the twofold axis (C_{2v}) with potential barrier of $\kappa - E_{ZP}$ to overcome, there exist two states $1A_1(A_{1g})$ and $1B_1(T_{1u})$ that become parallel, two perpendicular states $B_2(T_{1u})$ and $2A_1(T_{1u})$, and two states $3A_1(E_g)$ and $2B_1(E_g)$ becoming antiparallel. The former antiparallel state turns over at $\omega \approx 11$ and the latter at $\omega \approx 15$.

The dependence of the orientation cosine on the external field strength ω is shown in Fig. 7. Similar results as for the alignment, see Fig. 4, are obtained for the thermally averaged degree of orientation denoted as $\langle\langle \cos\theta \rangle\rangle$. We find the cooperative effect for field direction in $\langle 100 \rangle$ of the crystal with higher orientation for increasing crystal-field strength κ. In contrast, the external field competes with the crystal field in the other two cases leading to reduced orientation for increasing κ. In the left column of Fig. 7, where field is applied in $\langle 100 \rangle$ direction, the three curves for $\kappa = 5$, 25, and 50 are above the gas phase result, whereas in the other two panels the orientation cosines are below the gas phase value for $\omega \gtrsim 5$. For the higher temperature the result is rather independent of κ, as seen from the overlapping dashed lines. In all of these cases the thermal averages show that a low temperature is necessary for attaining a significant effect. The highest orientation of molecules is achieved when only the lowest parallel states are populated, e.g., for $\mathcal{T} = 1\, k_B/B$. At the higher temperature, $\mathcal{T} = 10\, k_B/B$, achieving high orientation is hampered by population of perpendicular and antiparallel states.

Provided that specific states can be populated initially, also weak fields $\omega \leq 1$ can be very effective in creating the orientation, as shown previously for the gas phase [18–23]. There it is shown, that parallel and antiparallel combinations are formed from a gerade–ungerade pair of states immediately for $\omega \neq 0$, by means of tunneling. This pseudo-first-order effect is

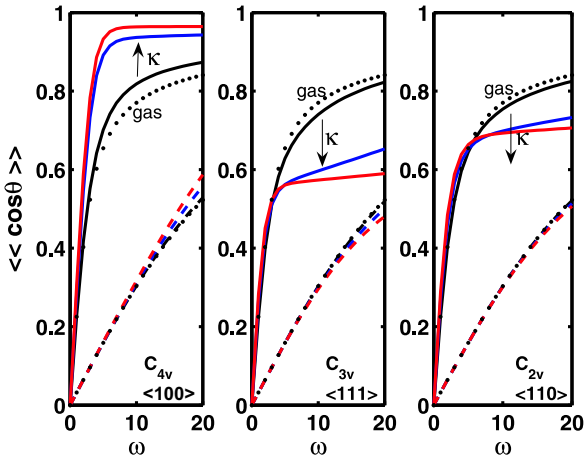

FIG. 7: (Color online) The degree of orientation thermally averaged $\langle\langle \cos\theta \rangle\rangle$ when the field (V_μ) is applied in three directions and for three crystal-field strengths $\kappa = 5$, 25, 50 as well as for the gas phase (points). Solid lines: $\mathcal{T} = 1\,k_\mathrm{B}/B$, dashed lines: $\mathcal{T} = 10\,k_\mathrm{B}/B$.

also present for interactions of V_κ and V_μ in the crystal fields investigated here, see the first and third rows in Table V. The dependence of tunneling splitting as a function of κ is shown in upper panel of Fig. 8. The A_{1g}–T_{1u} and T_{1u}–E_g energy splittings decrease exponentially from $2B$ and $4B$ at $\kappa = 0$ to $3.9 \times 10^{-4}B$ and $1.9 \times 10^{-4}B$ at $\kappa = 200$, respectively. At the same time, the crystal-field splitting increases to $54B$. We present orientation cosines with weak fields (low ω's) in lower panel of Fig. 8 for the case of cooperative interactions, i.e., for electrostatic field along a $\langle 100 \rangle$. Together with the increasing expectation value of $\cos\theta$ for the lowest state, A_1 (solid lines), we present the opposite result for the antiparallel component $3A_1$ by dashed lines. Increasing the strength of the crystal field reduces the tunneling splitting (see also Fig. 2) and thus enhances the field-induced couplings within the tunneling multiplet, as seen by the orientation cosines in Fig. 8. The parallel and antiparallel states formed thereby can split strongly apart already for low ω, achieving near unity orientation. For instance, the angular amplitude is narrowed to $\pm 11^\circ$ with $\omega = 1$ and $\kappa = 200$ for either of the states. The orientation effect vanishes in thermal averaging for $\omega < 1$ as the field strengths are no longer sufficient to separate levels in energy and to overcome the effect of Boltzmann statistics.

To conclude our investigation of orientation, we find similar results as for laser-induced alignment: High orientation is reached for combined internal (crystal) and external static

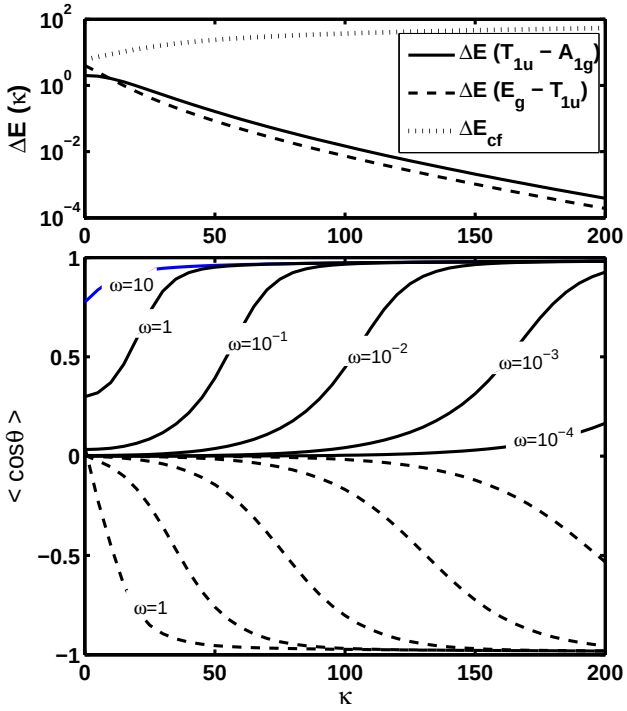

FIG. 8: (Color online) State specific orientation in the cooperative case (C_{4v}): $\langle\cos\theta\rangle(\kappa)$ for the lowest, parallel A_1 state (solid curves) with $\omega = 10$–10^{-4} and for the antiparallel $3A_1$ state (dashed curves) with $\omega = 1$–10^{-4}. The upper panel shows dependence of tunneling splittings ΔE between the indicated lowest octahedral states on the crystal-field parameter κ. The crystal-field splitting $\Delta E_{\rm cf}$ defined as $E(1T_{2g}) - E(1A_{1g})$ is also shown, see Fig. 2.

fields. While high fields are necessary if the effect of thermal averaging is included, very weak fields are sufficient to reach that goal for the ground state only. In particular, these fields are orders of magnitude smaller than needed for pendular orientation of gas phase molecules. These findings can be regarded as the solid state analog (V_κ+V_μ interaction) for the enhanced orientation in gas phase (V_α+V_μ). Differences, however, arise from the higher dimensionality. While in the gas phase the orientation is achieved by essentially one-dimensional tunneling between parallel and antiparallel directions, in the solid also perpendicular flips contribute.

VI. SUMMARY

We have assessed within a simplified model the problem of controlling the directionality of a linear molecule trapped in a cubic crystal. The rotational density distribution dictated by the octahedral crystal field is manipulated by the interaction with a laser or an electrostatic field to achieve alignment or orientation with respect to the polarization vector of the field, respectively. The potential energy curvature restricting the molecular rotation is higher in these solids than in the previously studied applications of the combined fields in gas phase. Thereby the directional structure of the states is more complex and a wider range of properties prevails. In particular, two reference frames for the molecule are present; there is a competition between the crystallographic axes and the direction of the external field. When the directions preferred by the fields coincide, we find cooperative effects for both alignment and orientation. In this case, it is possible to exceed the degree of angular confinement obtainable in gas phase. It is also shown that despite the competition between the internal and external fields, rotational densities can be manipulated at will — also to occupy directions maximally repelled by the crystal field, however, to a lower extent. This selectivity opens up a possibility to study direction-dependent reaction dynamics in solids.

The efficiency of the alignment and orientation schemes presented is affected by thermal conditions. The values of field strength parameters $\Delta\omega$ and ω are limited from below to accommodate a reasonable thermal population difference on the separated molecular states. Hence, using very weak fields for pseudo-first-order Stark effect on orientation is sufficient only in very favorable cases. Nevertheless, we find it comforting that the examined high ω range can be realized in future applications to experimentally show this effect in rare gas matrices. Furthermore, the question of selectively exciting individual field-induced states is currently under investigation. For that purpose, we are extending the present studies by taking the time dependence of the external fields explicitly into account. At the same time, the dissipative response of the matrix is handled by allowing distortions and adding the dependence on the translational and vibrational coordinates.

Experimental realization of the molecular alignment and orientation in solids depends on interplay of the molecular parameters B, $\Delta\alpha$, and μ. Typical parameters can be found, e.g., in Ref. [19]. Recently, we studied the ClF molecule ($B = 0.5165$ cm^{-1}, $\Delta\omega = 27$ at 1 TW/cm^2 field intensity, and $\omega = 3$ at 100 kV/cm field strength) in Refs. [43, 44], where

also the interaction with the matrix was estimated. Other work giving explicit values of κ can be found from spectroscopy [32, 39, 51–53] and modelling [35, 49, 54] of librational states. Experimental verification of the schemes as proposed in the present work poses a significant challenge. In the gas phase, ionization and subsequent time-of-flight [4, 20–23] or ion-imaging [55–58] measurements have been carried out to map the fragment atom directions in a molecule after the control pulses. In a solid, the detection must preferentially rely on optical responses only. For instance, the optical Kerr effect, which has been used for nonintrusive probing of alignment of gas phase molecules [59–61], deserves attention. First, before applying the control schemes, one must define the laboratory–crystal axes system so that one knows which field polarization directions coincide with the maxima of the rotational density. For macroscopic single crystals like doped alkali halides the symmetry planes are evident. For rare gases the free-standing crystal samples are polycrystalline. To reach the local symmetry, we can use a two-photon resonant excitation, thus selecting a $\cos^4\theta$ distributed subset of molecules, vary the polarization direction of the excitation field with respect to the sample crystal, and detect a modulation in the emission intensity. A micrometer-tight focusing is needed to sample a single grain and to prevent directional averaging.

For the nonresonant alignment, we need also a tight focus of the laser pulse in creating the high intensities. Here the destruction limits of the rare gas crystal pose a severe obstacle. Probing the anisotropy created in the sample by alignment and/or static fields remains then the ultimate goal and perhaps the most demanding stage of the experiment. In general we aim at using three-pulse schemes, where the alignment pulse (or set of pulses) is followed by a pump–probe excitation of electronic states and subsequent emission is detected as the polarization dependent signal. Electronic excitations however complicate matters due to coupling with the environment. The impulsive change to a degenerate Π state of the molecule leads to nontotally symmetric changes of the local cage symmetry by the Jahn–Teller effect, and the generated vibrational wave packet on the excited state potential further interacts with the surrounding atoms possibly leading to a depolarization effects which must be taken into account.

In an application stage we aim at the following: (i) We grow the crystal with a static electric field $\mathcal{E}_\mathrm{S}$ switched on to create a biased sample of dopant dipoles trapped in the lattice sites of the host. (ii) We apply the alignment field with polarization in an angle with respect

to $\mathcal{E}_S$ and detect the dynamics of a vibrational wave packet by pump–probe techniques and investigate the possibility to control dissociation and recombination yields. (iii) We switch the orientation field $\mathcal{E}_S$ off and investigate transition times for phonon-assisted tunneling by detecting a population rise perpendicular and a decay parallel to the switched bias field.

Acknowledgment

This research is funded by the project *Analysis and control of ultrafast photoinduced reactions* (SFB 450) of the Deutsche Forschungsgemeinschaft (DFG). T. K. is supported by the Academy of Finland.

---

[1] H. J. Loesch, Annu. Rev. Phys. Chem. **46**, 555 (1995).

[2] H. Guo and T. Seideman, Phys. Chem. Chem. Phys. **1**, 1265 (1999).

[3] T. Seideman, J. Chem. Phys. **115**, 5965 (2001).

[4] D. M. Villeneuve, S. A. Aseyev, P. Dietrich, M. Spanner, M. Y. Ivanov, and P. B. Corkum, Phys. Rev. Lett. **85**, 542 (2000).

[5] M. Yamaki, K. Hoki, Y. Ohtsuki, H. Kono, and Y. Fujimura, Phys. Chem. Chem. Phys. **7**, 1900 (2005).

[6] J. Itatani, J. Levesque, D. Zeidler, H. Niikura, H. Pépin, J. C. Kieffer, P. B. Corkum, and D. M. Villeneuve, Nature **432**, 867 (2004).

[7] H. Stapelfeldt, Nature **432**, 809 (2004).

[8] T. Kanai, S. Minemoto, and H. Sakai, Nature **435**, 470 (2005).

[9] J. P. Marangos, Nature **435**, 435 (2005).

[10] H. Stapelfeldt and T. Seideman, Rev. Mod. Phys. **75**, 543 (2003).

[11] B. Friedrich and D. Herschbach, Phys. Rev. Lett. **74**, 4623 (1995).

[12] B. Friedrich and D. Herschbach, J. Phys. Chem. **99**, 15686 (1995).

[13] T. Seideman, J. Chem. Phys. **103**, 7887 (1995).

[14] T. Seideman, J. Chem. Phys. **106**, 2881 (1997).

[15] J. J. Larsen, K. Hald, N. Bjerre, H. Stapelfeldt, and T. Seideman, Phys. Rev. Lett. **85**, 2470 (2000).

[16] W. Kim and P. M. Felker, J. Chem. Phys. **104**, 1147 (1996).

[17] W. Kim and P. M. Felker, J. Chem. Phys. **108**, 6763 (1998).

[18] B. Friedrich and D. Herschbach, J. Chem. Phys. **111**, 6157 (1999).

[19] B. Friedrich and D. Herschbach, J. Phys. Chem. A **103**, 10280 (1999).

[20] S. Minemoto, H. Nanjo, H. Tanji, T. Suzuki, and H. Sakai, J. Chem. Phys. **118**, 4052 (2003).

[21] H. Sakai, S. Minemoto, H. Nanjo, H. Tanji, and T. Suzuki, Phys. Rev. Lett. **90**, 083001 (2003).

[22] N. H. Nahler, R. Baumfalk, U. Buck, Z. Bihary, R. B. Gerber, and B. Friedrich, J. Chem. Phys. **119**, 224 (2003).

[23] B. Friedrich, N. H. Nahler, and U. Buck, J. Mod. Optic. **50**, 2677 (2003).

[24] B. Friedrich and D. R. Herschbach, Nature **353**, 412 (1991).

[25] H. Bethe, Ann. Phys. **3**, 133 (1929).

[26] L. Pauling, Phys. Rev. **36**, 430 (1930).

[27] A. F. Devonshire, Proc. R. Soc. London, Ser. A **153**, 601 (1936).

[28] V. Narayanamurti and R. O. Pohl, Rev. Mod. Phys. **42**, 201 (1970).

[29] T. Kiljunen, B. Schmidt, and N. Schwentner, Phys. Rev. Lett. **94**, 123003 (2005).

[30] H. E. Hallam, ed., *Vibrational Spectroscopy of Trapped Species* (Wiley, London, 1973).

[31] L. Andrews and M. Moskovits, eds., *Chemistry and Physics of Matrix–Isolated Species* (North–Holland, Amsterdam, 1989).

[32] C. E. Mungan, U. Happek, J. T. McWhirter, and A. J. Sievers, J. Chem. Phys. **107**, 2215 (1997).

[33] K. Nishidate, M. Baba, Sarjono, M. Hasegawa, K. Nishikawa, I. Sokolska, and W. Ryba-Romanowski, Phys. Rev. B **68**, 224307 (2003).

[34] I. Holleman, G. von Helden, A. van der Avoird, and G. Meijer, Phys. Rev. Lett. **80**, 4899 (1998).

[35] T. Yildirim and A. B. Harris, Phys. Rev. B **66**, 214301 (2002).

[36] H. Friedmann and S. Kimel, J. Chem. Phys. **43**, 3925 (1965).

[37] H. Friedmann and S. Kimel, J. Chem. Phys. **47**, 3589 (1967).

[38] J. Manz, J. Am. Chem. Soc. **102**, 1801 (1980).

[39] V. Berghof, M. Martins, B. Schmidt, and N. Schwentner, J. Chem. Phys. **116**, 9364 (2002).

[40] S. Estreicher and T. L. Estle, Phys. Rev. B **30**, 7 (1984).

[41] S. Hennig, A. Cenian, and H. Gabriel, Chem. Phys. Lett. **205**, 354 (1993).

[42] Z. Li and V. A. Apkarian, J. Chem. Phys. **107**, 1544 (1997).

[43] T. Kiljunen, M. Bargheer, M. Gühr, and N. Schwentner, Phys. Chem. Chem. Phys. **6**, 2185 (2004).

[44] T. Kiljunen, M. Bargheer, M. Gühr, N. Schwentner, and B. Schmidt, Phys. Chem. Chem. Phys. **6**, 2932 (2004).

[45] R. N. Zare, *Angular momentum* (John Wiley & Sons, New York, 1988).

[46] B. Schmidt and P. Žďánská, Comput. Phys. Commun. **127**, 290 (2000).

[47] E. B. Wilson, Jr., J. C. Decius, and P. C. Cross, *Molecular vibrations* (Dover, New York, 1955).

[48] C. J. Bradley and A. P. Cracknell, *The mathematical theory of symmetry in solids* (Clarendon, Oxford, 1972).

[49] H. U. Beyeler, J. Chem. Phys. **60**, 4123 (1974).

[50] G. K. Pandey, K. L. Pandey, M. Massey, and R. Kumar, Phys. Rev. B **34**, 1277 (1986).

[51] L. Khriachtchev, A. Lignell, J. Juselius, M. Räsänen, and E. Savchenko, J. Chem. Phys. **122**, 014510 (2005).

[52] V. A. Apkarian and E. Weitz, J. Chem. Phys. **76**, 5796 (1982).

[53] W. H. Flygare, J. Chem. Phys. **39**, 2263 (1963).

[54] G. K. Pandey, M. Massey, K. L. Pandey, and R. Kumar, Phys. Rev. B **39**, 10300 (1989).

[55] J. J. Larsen, H. Sakai, C. P. Safvan, I. Wendt-Larsen, and H. Stapelfeldt, J. Chem. Phys. **111**, 7774 (1999).

[56] F. Rosca-Pruna and M. J. J. Vrakking, Phys. Rev. Lett. **87**, 153902 (2001).

[57] F. Rosca-Pruna, E. Springate, H. L. Offerhaus, M. Krishnamurthy, N. Farid, C. Nicole, and M. J. J. Vrakking, J. Phys. B **34**, 4919 (2001).

[58] E. Péronne, M. D. Poulsen, H. Stapelfeldt, C. Z. Bisgaard, E. Hamilton, and T. Seideman, Phys. Rev. A **70**, 063410 (2004).

[59] V. Renard, M. Renard, S. Guérin, Y. T. Pashayan, B. Lavorel, O. Faucher, and H. R. Jauslin, Phys. Rev. Lett. **90**, 153601 (2003).

[60] V. Renard, M. Renard, A. Rouzée, S. Guérin, H. R. Jauslin, B. Lavorel, and O. Faucher, Phys. Rev. A **70**, 033420 (2004).

[61] J. G. Underwood, M. Spanner, M. Y. Ivanov, J. Mottershead, B. J. Sussman, and A. Stolow, Phys. Rev. Lett. **90**, 223001 (2003).